A laboratory experimental technique for simulating combined blast and impact loading

Lang Li , Qian-Cheng Zhang , Rui Zhang , Wang Xin , Zhen-Yu Zhao , Si-Yuan He , Bin Han , Tian Jian Lu

PII: S0734-743X(18)31099-6
DOI: https://doi.org/10.1016/j.ijimpeng.2019.103382
Reference: IE 103382

To appear in: *International Journal of Impact Engineering*

Received date: 30 October 2018
Revised date: 7 July 2019
Accepted date: 20 August 2019

Please cite this article as: Lang Li , Qian-Cheng Zhang , Rui Zhang , Wang Xin , Zhen-Yu Zhao , Si-Yuan He , Bin Han , Tian Jian Lu , A laboratory experimental technique for simulating combined blast and impact loading, *International Journal of Impact Engineering* (2019), doi: https://doi.org/10.1016/j.ijimpeng.2019.103382

Highlights

- A novel composite projectile for simulating combined blast and impact loading has been proposed.
- The composite-projectile-based approach is proved to be valid in simulating combined loadings from cased explosives under certain conditions.
- Based on the experimental approach, a new synergetic effect of combined blast and single fragment impact loading is found.
- The proposed approach provides a chance to investigate ballistic impact of deforming target experimentally.

A laboratory experimental technique for simulating combined blast and impact loading

Lang Li[a,b], Qian-Cheng Zhang[a,c*], Rui Zhang[a,b], Wang Xin[a,b], Zhen-Yu Zhao[a,b], Si-Yuan He[e], Bin Han[d], Tian Jian Lu[b,a,*]

[a]*State Key Laboratory for Strength and Vibration of Mechanical Structures, Xi'an Jiaotong University, Xi'an 710049, P.R. China*

[b]*State Key Laboratory of Mechanics and Control of Mechanical Structures, Nanjing University of Aeronautics and Astronautics, Nanjing 210016, P.R. China*

[c]*Key Laboratory of Intense Dynamic Loading and Effect, Xi'an, 710024, P.R. China*

[d]*School of Mechanical Engineering, Xi'an Jiaotong University, Xi'an 710049, PR China*

[e]*State Key Laboratory of Bioelectronics, School of Biological Science & Medical Engineering, Southeast University, Nanjing 210096, China*

Abstract

A novel composite projectile is put forward to simulate combined blast and single fragment impact loading, which is comprised of a cylindrical aluminum foam projectile embedded with a fragment simulation projectile (FSP). Comparison between cased explosive and composite projectile in terms of the generated combined loading shows that the composite projectile technique is theoretical feasible. Experimental tests for normal impact of the composite projectile on clamped plates are carried out. Results show that the proposed composite projectile

*Corresponding authors: zqc111999@ xjtu.edu.cn(QCZ); tjlu@nuaa.edu.cn (TJL).

can induce both blast-induced deflection and fragment-induced perforation on the clamped plate. The arrival time interval between blast and fragment has significant influence on the extent of induced damage on the plate and the residual FSP velocity. Numerical simulations with the method of finite elements are carried out to provide further insight into the interaction between the composite projectile and clamped plate, and to explain observations and measurements in experiments. The present study reveals a new synergetic effect of combined blast and single fragment impact loading on clamped plate: arrival time interval between blast and impact loading affects significantly the residual velocity of the FSP.

Keywords: *Composite projectile; Metal foam; Blast loading; Single fragment impact loading; Synergetic effect.*

1 Introduction

Cased explosives such as improvised explosive devices (IEDs) and roadside bombings pose serious threat to both military and civilian vehicles in numerous conflict areas [1-4]. Once the charge inside of the casing is detonated, combined loading caused by blast and fragmentation impact is generated, causing synergetic damage to the vehicles [5, 6]. On one side, fragments produced by metal casing may perforate the surrounding structures; on the other hand, blast loading caused by the propagation of blast wave would aggravate the structural damage. The synergetic effects of these two destructive loadings have become the subject of a

number of ongoing researches.

To study the effects of combined blast and fragment loading on the response of reinforced concrete structures, a numerical method was proposed [7], with the synergetic effects artificially decoupled into blast loading and fragment loading. It was demonstrated that damage caused by the combined loading was more severe than the sum of damages caused by the blast and fragment loading alone. Also using numerical approaches, Ebrahimi *et al.* [8] and Zhang *et al.* [9] investigated the response of honeycomb-core and I-core sandwich plates subjected to combined blast and fragment loading, respectively, which expand the investigation of structures under combined blast and fragment loading from monolithic plates to sandwich structures. Although numerical simulations can capture many of the phenomenological details of the combined blast and fragment loading, such as the contact force time histories between composite projectiles and targets, the velocity time histories of the projectiles, and the stress state of the targets, experimental investigation is much needed to find new phenomena and to validate the numerical simulations.

At present, concerning the synergetic effects of combined blast and fragment loading, only a limited number of experimental studies have been reported. For typical instance, Li *et al.* [10] experimentally investigated the deformation and damage characteristics of monolithic steel plates under combined blast and fragment loading by detonating fragments covered TNT. The results revealed that the penetrability of fragment cluster is the key factor for the occurrence of a visible penetration hole in the central region of the plate. Performing experiments is

nonetheless costly. Further, experimentally, it is not easy to explore the physical mechanisms underlying the synergetic effects of combined blast and fragment loading for there are numerous randomly distributed fragments. Rakvag *et al*. [11] simplified the experiments by idealizing the perforations as pre-formed holes of generalized shapes in the target steel plates; subsequently, they applied controlled pressure pulses on the plates, aiming at providing insight into the combined effects of pressure and fragment loading. However, this methodology is only applicable to the situation wherein the fragments strike and perforate the target before the blast wave arrives. Therefore, there is pressing need to develop a simple, economical and safe experimental technique to dynamically load a structure and generate the synergetic effects of combined blast and fragment impact.

Alternative laboratory methods for simulating extreme loading events are attractive for detailed parametric studies. Previously, an experimental technique to subject structures to high intensity pressure pulses was successfully developed using metal foam projectiles [12], which has been widely employed to investigate the shock resistance of sandwich structures [13-16]. Subsequently, Park *et al.* [17-20] developed an apparatus to launch high-speed sand slugs against structures to simulate localized loading on structures by ejecta from landmine explosion. Motivated by these experimental studies, a novel laboratory experimental technique on the basis of a composite projectile is proposed in the current study to simulate combined blast and single fragment impact loading. With reference to Fig. 1, the composite projectile is comprised of a fragment simulation projectile (FSP) embedded in a cylindrical metal

foam projectile. The foam projectile and the FSP have length L and l, respectively. The depth of the inner hole is defined as Δd, while the diameter of the foam projectile, the FSP and the inner hole is D, d_1 and d_2, respectively. When the composite projectile impinges on a target with prescribed velocity V_0, combined loading is applied on the target. Note that the focus of the study is placed upon the combined loading of blast and individual fragment impact, rather than fragments cluster.

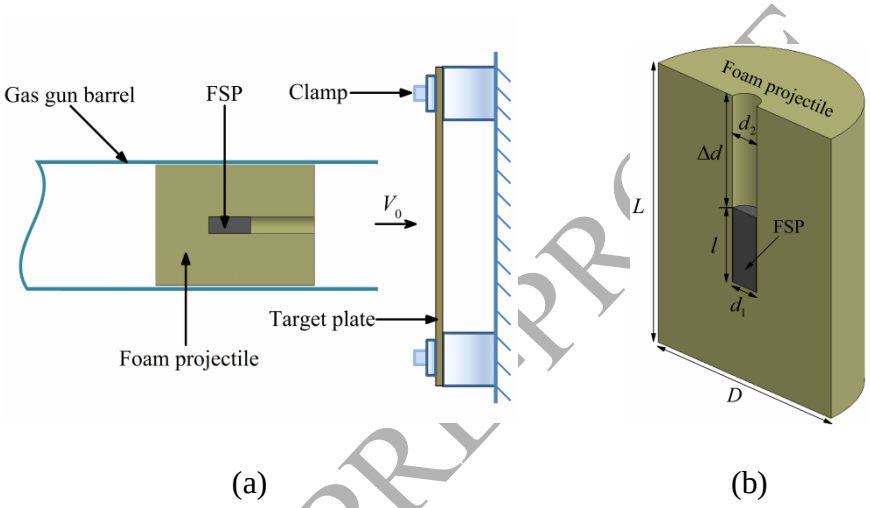

Fig.1 (a) Schematic of laboratory experimental technique using composite projectile to generate combined shock and fragment; (b) cross-sectional view of composite projectile. FSP: fragment simulation projectile.

The paper is structured as follows. Section 2 presents the characteristics of combined blast and fragment loading and the theoretical framework of the proposed laboratory experimental technique. In Section 3, the experimental program is presented and the procedure of measurements outlined. In Section 4, the synergetic effects of combined blast and single fragment impact loading are investigated based on the proposed experimental tool. Finally, in Section 5, numerical simulations based on the method of finite elements (FE) are carried out to explain the observations and

measurements from experiments.

2 Theoretical framework

2.1 The characteristics of combined blast and fragment loading

When the detonation of explosive filler in a cased bomb is initiated, the inside temperature and pressure increase rapidly such that the casing expands until it breaks up in fragments. The energy remaining after swelling and fragmenting of the casing imparts velocity to the fragments, which expand into the surrounding air. A structure nearby is thus exposed to both blast and fragments loading [7]. The combined loading of blast and fragments exhibits three main characteristic stages: impulse load from the blast wave, impulse load and perforation from the striking fragments.

2.1.1 Blast loading

Typically, the pressure-time profile at a fixed point in space for a blast wave resulting from an uncased charge in free air decays exponentially [21, 22, 23]. Assume the detonation takes place at time $t = 0$ and the blast wave arrives at the fixed point at time $t = t_a^b$. As the blast wave arrives, the pressure increases from ambient pressure to the peak pressure due to high compression of the air by the incident over-pressure. The incident over-pressure is dependent upon the material make of the explosive, the mass (C) of the explosive, and the standoff distance (r) between the explosive and the target surface. For a given explosive, the peak pressure (ΔP_i) of the incident blast wave can be approximated by [22]:

$$\Delta P_i\left(\bar{r}\right)=\begin{cases}\left(\dfrac{0.67}{\bar{r}^3}+\dfrac{3.01}{\bar{r}^2}+\dfrac{4.31}{\bar{r}}\right)\times10^5\ Pa\ \ 0.5\le\bar{r}\le70.9\\ \left(\dfrac{0.00625}{\bar{r}^4}-\dfrac{0.3572}{\bar{r}^3}+\dfrac{5.5397}{\bar{r}^2}+\dfrac{14.0717}{\bar{r}}\right)\times10^5\ Pa\ \ 0.05\le\bar{r}\le0.5\end{cases} \tag{1}$$

where $\bar{r}=r/\sqrt[3]{C}$.

When the incident pressure encounters a surface, it is reflected and amplified with a reflection coefficient C_R ranging from 2 to 8 according to Eq. (2), which is derived from the Rankine-Hugoniot (or the shock jump) relationship and is written as [24]:

$$C_R=\frac{14+8\left(\Delta P_i/P_0\right)}{7+\left(\Delta P_i/P_0\right)} \tag{2}$$

where P_0 is the ambient pressure. The reflected peak pressure should thus be $\Delta P_r=C_R\cdot\Delta P_i$. The action time of the pressure on a structure can be approximated as:

$$t^+=1.35\times10^{-3}\sqrt{r}\sqrt[6]{C} \tag{3}$$

For cased charges, the casing effect should be considered. Taking the casing effect directly into account is difficult, but an alternative method by giving the equivalent bare charge that will yield the same impulse as the cased charge at the same distance is provided by Hutchinson [25]. According to the Hutchison model, the equivalent charge mass C_e is evaluated as follows:

$$C_e=C\sqrt{\frac{0.5}{0.5+M/C}} \tag{4}$$

where M is the mass of the casing. Under this situation, to calculate the peak pressure and action time, the charge mass C in Eqs. (1) and (3) should be replaced by the equivalent charge mass C_e.

2.1.2 Fragment loading

As the charge inside of the casing is detonated, the casing swells due to high pressure. During swelling, cracks form and propagate in the casing until fragments are formed [26]. As detailed expressions of the fragmentation are complex, in the present study, an single fragment is considered.

The initial velocity of the fragment V_{Gurney} can be predicted using the Gurney equation derived from an assumption of cylindrical charge, as [27]:

$$V_{Gurney} = \sqrt{2E}\sqrt{\frac{C/M}{1+0.5C/M}} \tag{5}$$

where $\sqrt{2E}$ is the empirical 'Gurney constant', taken as 2316 m/s for TNT. As the fragment travels through air, its velocity gradually decreases due to the drag force. The velocity reduction can be predicted by [24]:

$$\frac{V_f(r)}{V_{Gurney}} = e^{-\beta\frac{r}{m_f^{1/3}}} \tag{6}$$

where $\beta = 0.004$ and m_f is the fragment mass.

In the present study, the mass of the single fragment is taken as the 'average fragment' mass as representative, *i*.e., the average mass of all fragments is given by:

$$m_f = 2\mu \tag{7}$$

where $\mu = \beta^2 h_0^{5/3} D_0^{2/3}(1+h_0/D_0)^2$ is a fragments distribution parameter with $\beta = 3.81\,\mathrm{kg}^{1/2}/\mathrm{m}^{7/6}$ for TNT. h_0 and D_0 are the thickness and inner diameter of cylinder casing, respectively [24].

2.1.3 Arrival time

Since the propagation velocity of the blast wave (V_b) is different from the flying velocity of the fragment (V_f), the arrival time of the two loadings needs to be considered. The velocity of shock wave in air can be approximated as [22]:

$$V_b(r) = \sqrt{\left[(k+1)\Delta P_i(r) + 2kP_0\right]/2\rho_0} \tag{8}$$

where P_0 and ρ_0 are the ambient pressure and the density of air, respectively, and $k = 1.4$ is the adiabatic exponent. It should be noted that Eq. (8) is based on the plane shock wave assumption and the temperature effects are not taken into consideration. Thus, the arrival time of the blast wave in free air, t_a^b, can be obtained by integrating (8) against time.

The arrival time of the fragment (mass m_f) is calculated by solving first the differential equation (upon substituting $V_f(t) = dr/dt$) for $r(t)$ that satisfies the condition $r(t=0) = 0$. For a given r, t_a^f can then be solved numerically. In applications where the distance is relatively small (< 1 m), the velocity reduction is less than 1%, so the arrival time of fragment can be approximated as:

$$t_a^f = 2r/\left(V_{Gurney} + V_f(r)\right) \tag{9}$$

Finally, the time interval between the arrival time of blast wave and fragment is obtained as:

$$\Delta t = t_a^f - t_a^b \tag{10}$$

2.1.4 Predictions of the combined loadings

Thus far, the characteristics of combined blast and single fragment impact loading are presented using both theoretical and empirical formulas, which have been validated experimentally in many studies [5, 6]. Therefore, in what follows, the formulas are employed directly. Since the aim of the present study is to simulate the combined loading of blast and single fragment impact, the distribution of fragments and their corresponding velocities are not considered. For illustration, Fig. 2 plots the arrival times of blast and a single fragment (mass m_f) as functions of the standoff distance for 16 kg charge filled with 50% TNT, as predicted using Eqs. (1) to (10). Initially, the blast wave arrives before the fragment until they meet at the standoff distance of 3.7 m. Afterwards, as the standoff distance is increased, the fragment arrives before the blast wave. The results of Fig. 2 also reveal that the action time t^+ is longer than the time interval Δt. Therefore, when $0 \le \Delta t < t^+$, the blast wave and fragment generate synergetic effects. Actually, when $\Delta t < 0$, the synergetic effects could still be triggered due to the interaction between the fragment and blast loading, but the current experimental set-up can not take this case into consideration.

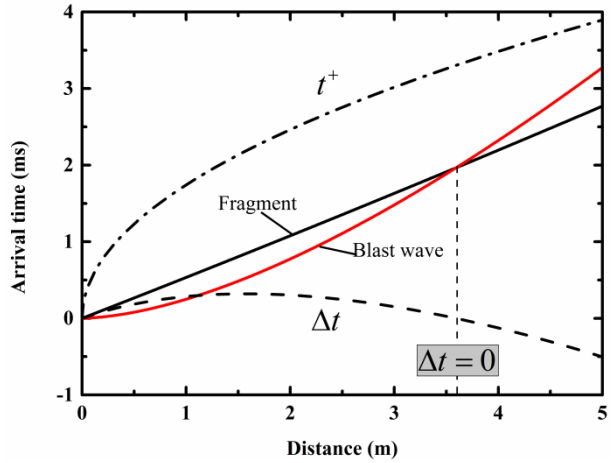

Fig. 2. Predicted arrival times of blast and fragment plotted as functions of standoff distance for 16-kg charge filled with 50% TNT.

2.2 Direct impact model of composite projectile

Experimentally, it has been well established that high velocity impact of high porosity homogeneous metal foam projectiles can simulate shock loading [12]. With this approach, metal foam projectiles with length L and density ρ_f are fired from a high-pressure gas gun at velocity V_0, which produce pressure versus time pulses. Through appropriate selection of the foam projectile properties and velocity, pressure pulses representative of blast loading from actual explosions can be achieved [13]. The peak pressure caused by the interaction between the impinging foam projectile and the rigid target is [12]:

$$\Delta P = \sigma_c + \frac{\rho_f V_0^2}{\varepsilon_D} \tag{11}$$

and the duration is

$$\tau = \frac{L\varepsilon_D}{V_0} \tag{12}$$

where σ_c and ε_D are the plateau stress and nominal densification strain of the metal foam.

Motivated by the above approach, we consider a novel composite projectile, as shown in Fig. 1b. The composite projectile is consisted of metal foam projectile and FSP embedded in the cylindrically shaped inner hole of the foam front-end. The cylindrical foam projectile (density ρ_f) is used to generate shock pressure on the target, while the FSP made of hardened steel (density ρ_s) is used to simulate single fragment impact loading. With reference to Fig. 3, let the composite projectile impact against a rigid wall with an initial velocity of V_0 at $t=0$. To minimize the influence of the inner hole size on the foam projectile, the diameter of the inner hole should be much less than the diameter of the foam projectile ($D/d_1 \geq 7$ is suggested).

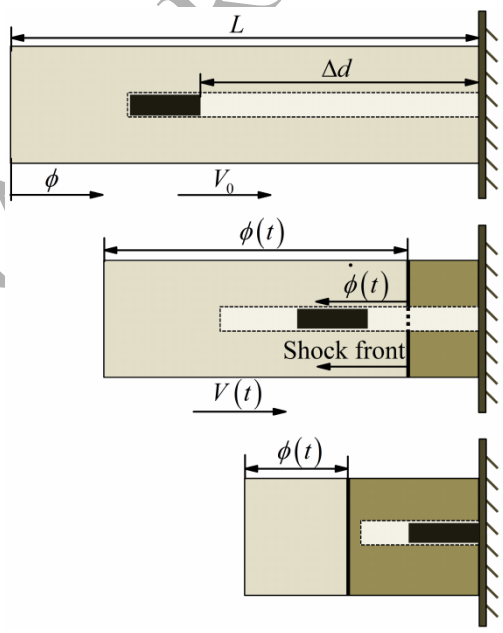

Fig. 3. Schematic of a composite projectile composed of foam projectile and fragment simulation projectile (FSP) impacting against a rigid wall.

The front-end of the foam impinges on the target first, resulting in compaction of

the foam projectile and reduction of its residual velocity. As the velocity of the foam projectile decreases, the FSP will be 'ejected' from the inner hole with initial velocity V_0, behaving as a fragment. Assuming the target is rigid, the time interval between the two loadings may be approximated as:

$$\Delta t = \frac{\Delta d}{V_0} \tag{13}$$

Since the ejected fragment is taken as one kind of kinetic projectile, the specific kinetic energy equivalence principle is adopted here to characterize the ejected fragment. As the density and velocity of the FSP are ρ_s and V_0, respectively, its specific kinetic energy is given by:

$$\overline{E} = \frac{\rho_s l V_0^{\,2}}{2} \tag{14}$$

2.3 Combined loadings from cased explosive and composite projectile: comparison

In the previous sections, it has been demonstrated that the proposed composite projectile can generate combined shock loading and impact loading. However, whether it is representative of combined blast and single fragment impact loading from cased explosives needs further verification. In the present section, the proposed implementation strategy of the composite projectile is validated. To this end, the geometry of a cylindrical cased charge is specified as follows: $C/M = 1$, $L_0/D_0 = 5$, $h_0/D_0 = 0.05$, where L_0 is the length of the cased charge. Fig. 4 plots the contours of the time interval between blast wave and fragment, the peak reflected pressure of blast

wave, and the specific kinetic energy of the single fragment with mass of m_f. The equivalent TNT mass serves as the *X*-axis and the detonation distance as the *Y*-axis. Thus, at each point (C_e, r) of Fig. 4, a group of parameters (Δt, ΔP_r, $\overline{E}$) is uniquely determined. (Note that regions with $\Delta t < 0$ are beyond the present consideration.) Whether a certain point can be simulated by the composite projectile mainly depends on the achieved parameters at the corresponding point by the purposely-designed projectile. For a composite projectile with given geometries of (l, Δd, L), material properties of (ρ_s, ρ_f, ε_D) and initial velocity V_0, the peak pressure, time interval and specific kinetic energy of the FSP can be determined by Eqs. (11), (13) and (14), respectively.

Take a gas gun with diameter of 57 mm and maximum projectile's flight velocity of 600 m/s for example. The length of the composite projectile should be shorter than 114 mm to avoid the vibration of the projectiles. Moreover the projectile velocity should be lower than 600 m/s. Restricted by these limitations above, the regions (in colorful background) in which the composite projectile can simulate combined blast and single fragment (mass m_f) loading of cased charges are approximately determined, as shown in Fig. 4. It can be seen that there exist two regions in which characteristics of combined loading at each point can be simulated by the composite projectile, i.e. the small one for polyurethane foam (with varying densities from 40 kg/m^3 to 60 kg/m^3) and the larger one for aluminum foam (with varying densities from 135 kg/m^3 to 405 kg/m^3). It should be noted that this is strictly plotted in Fig. 4 as a function of the equivalent TNT mass and the detonation distance

wherein the single fragment has a mass of m_f at each point. Actually, if the fragment is not restricted to the average fragment of the cased charge and the projectile velocity of gas gun is not limited, the composite projectile can be effectively used in more regions.

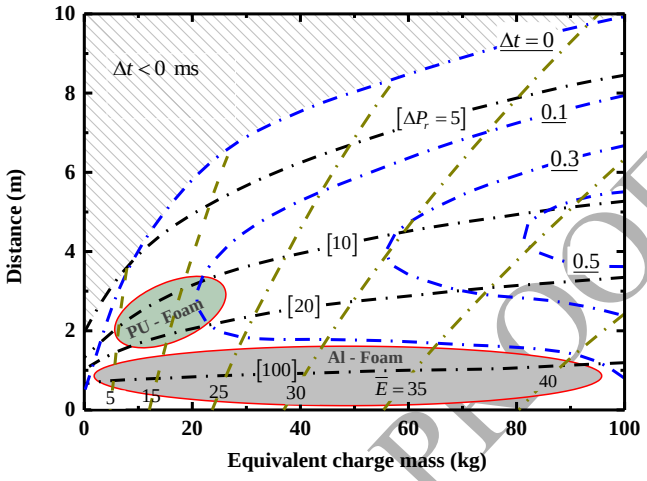

Fig. 4. Comparison between cased explosive and composite projectile in terms of characteristics of combined loading generated. Δt, ΔP_r, $\bar{E}$ have units of ms, MPa and MJ/m^2, respectively.

3 Experimental program

In the previous section, the potential of composite projectiles in simulating combined blast and single fragment impact loading has been theoretically validated. In this experimental section, we employ the composite projectile to generate normal impact on a clamped plate, aiming to: (i) verify the feasibility of the proposed method; (ii) investigate the synergetic damage caused by combined blast and single fragment impact loading.

3.1 Composite projectile

As shown in Fig. 5, the cylindrical composite projectile comprises of inner-holed aluminum foam with closed cells and the FSP. For simplicity, a blunt-nosed projectile made of 304 stainless steel is used to represent the FSP. The cylindrical foam of length $L = 85\,\text{mm}$ and diameter $D = 57\,\text{mm}$ are electro-discharge machined from a block of closed-cell aluminum foam with density $\rho_f = 369\,\text{kg/m}^3$. The aluminum foam was manufactured by coupling the processes of melt foaming and solidification [28]. The inner hole with depth Δd and diameter $d_2 \approx 8\,\text{mm}$ is also electro-discharge machined. The cylindrical FSP with $l = 20\,\text{mm}$ in length and $d_1 = 7.62\,\text{mm}$ in diameter is then inserted into the inner hole and glued in place by Vaseline. The diameter of the inner hole should be slightly larger than the FSP to avoid the resistance between the foam and FSP due to compression-expansion of the foam. In the current study, a small gap of 0.2 mm between foam and FSP is selected. For comparison, foam projectiles (without FSP and inner hole) having the same size as the composite projectiles ($L = 85\,\text{mm}$, $D = 57\,\text{mm}$) are also prepared.

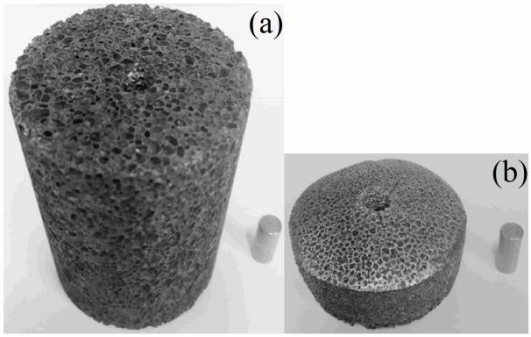

Fig. 5. Composite projectile: (a) before the impact test and (b) after the test.

3.2 Properties of constituent materials

The quasi-static compressive response of closed-cell aluminum foam is given in Fig. 6a, measured at a nominal strain rate of 0.0067 s^{-1} using cylindrical specimens of length 60 mm and diameter 37 mm. The foam displays a plateau strength of approximately 4.5 MPa and a nominal densification strain of $\varepsilon_D = 0.7$. The tensile stress versus strain curve of 304 stainless steel sheet (thickness 1.78 mm) is given in Fig. 6b, measured at a nominal strain rate of 10^{-3} s^{-1}.

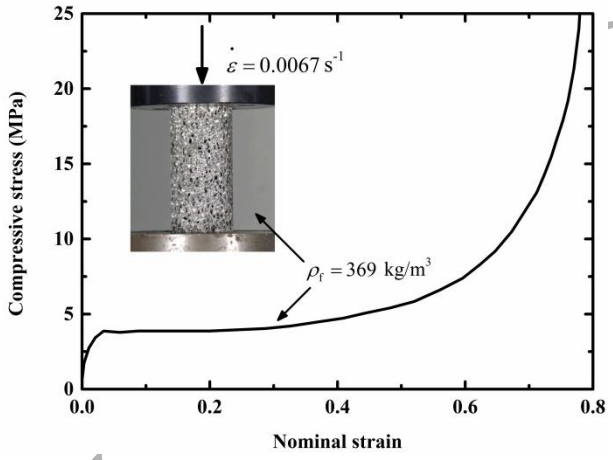

(a)

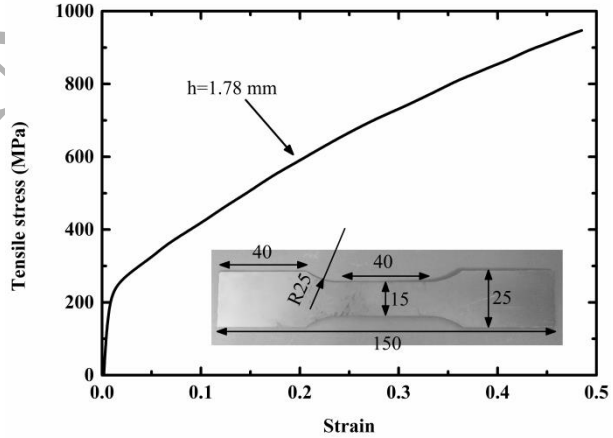

(b)

Fig. 6 (a) Quasi-static compressive stress versus strain curve of aluminum foam projectile and (b) quasi-static tensile response of 304 stainless steel sheet (all dimensions in mm).

3.3 Normal impact of a clamped plate

A series of experiments were performed to apply direct impact with the proposed composite projectile on fully-clamped target plates, as shown in Fig. 7. Each target plate is made of 304 stainless steel sheet (thickness 1.78 mm; plane size 100 mm by 100 mm). Twelve equally-spaced clearance holes for M8 bolts are drilled on the target plate on a pitch circle of radius 9 mm. The target plate is then clamped and fastened between a cover plate and a basing frame by M8 bolts (Fig. 7). Four different types of composite projectile and one type of foam projectile are employed for the impact test. Table 1 summaries the set of experiments performed and the details of composite projectiles used. The composite projectiles differ only in the depth of the inner hole.

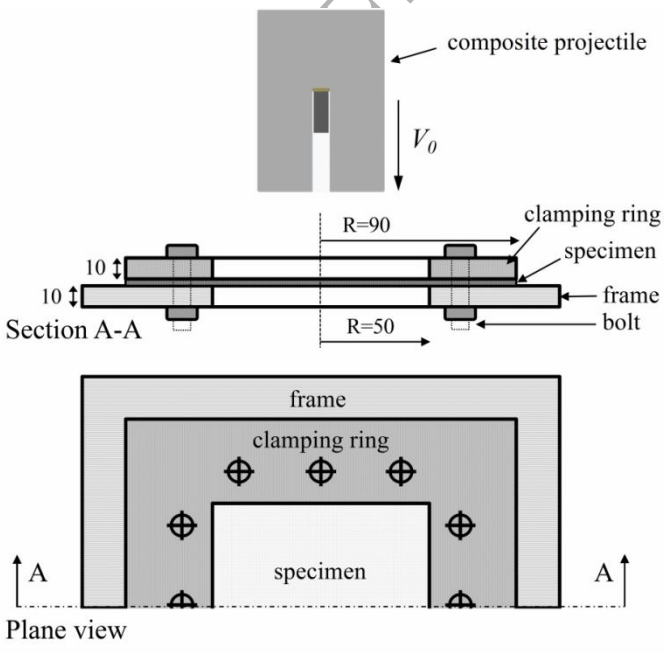

Fig. 7 Schematic of clamping arrangement for normal impact testing (all dimensions in mm).

Table 1

Summary of impact tests performed on clamped square monolithic plates. The specimens are labeled as S-*i*, where S denotes the specimen and *i* represents the type of loading characterized by the depth of inner hole ($\Delta d = i$ mm).

Specimen	ρ_f (kg/m^3)	Δd (mm)	V_0 (m/s)	V_r (m/s)	d_f (mm)	d_p (mm)
S-foam	375	-	324	-	27.5	-
S-0	371	0	319	224	30.5	8.3
S-10	363	10	315	168	45.7	36.7
S-20	377	20	317	203	40.1	15.9
S-30	368	30	325	245	28.2	7.7

4 Experimental results and discussion

Four levels of combined blast and single fragment impact loadings are applied to each specimen configuration by varying the inner hole depth Δd of the composite projectiles, as shown in Table 1. Table 1 also summarizes the observed permanent mid-span (central) deflection d_f, the perforation diameter of each specimen d_p and the measured residual velocity V_r of each FSP.

4.1 Observations

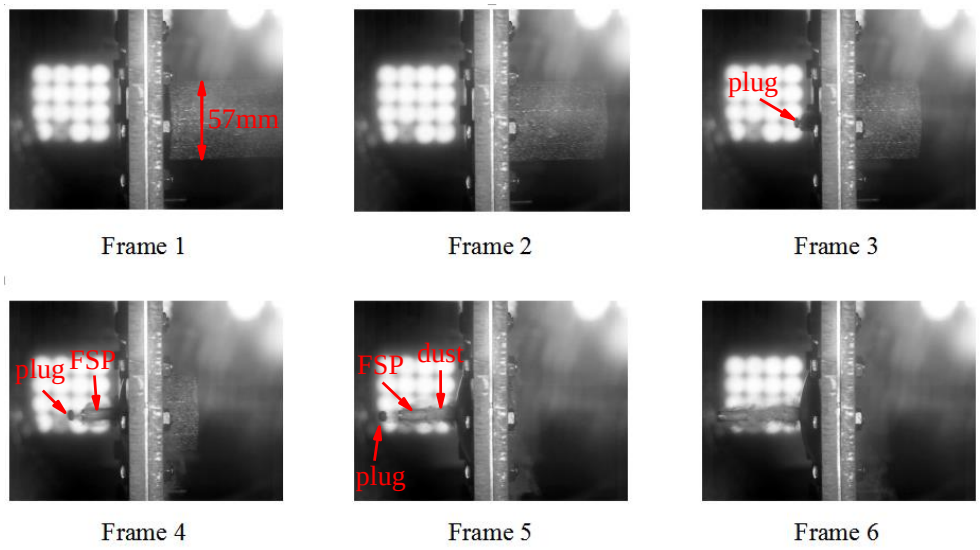

Fig. 8. High-speed photographic sequence at 0.075 ms intervals for specimen S-0.

Figure 8 displays a sequence of high-speed photographs at 0.075 ms intervals for the deformation of the specimen S-0. The impact occurs between Frame 1 and Frame 2, and by frame 3 the metal foam cylinder of the composite projectile is nearly 30% crushed (that is, axial length reduced by 30%) while the FSP has 'ejected' from the composite projectile and just perforated the monolithic plate. As the metal foam continues to be crushed, the FSP is wholly 'ejected' from the composite projectile, and a plug punched from the plate can be seen flying together with the FSP, as shown in Frame 4. Subsequently, the metal foam continues to impinge the plate while the FSP and the punched plug fly away from the plate, as seen in Frames 5 and 6. The dust cloud followed by the FSP shown in Frames 5 and 6 is caused by the pulverisation of metal foam upon uniaxial crushing as stated by [13].

Judging from the above experimental observations, we can infer that the plate is

first loaded by the meal foam, which leads to bending and stretching of the plate. It is then loaded simultaneously by both the metal foam projectile and the FSP wherein perforation of the plate is triggered. Subsequently, after the plate is perforated by the FSP, it is again loaded by the foam projectile which further stretches the plate. Since this whole process can not be observed directly, additional FE simulations are needed to show the interaction between composite projectile and target plate, especially the ejection process of the FSP from the inner hole and its impinging on the target plate. FE simulations are performed in Section 5.

4.2 Deformation/failure mode

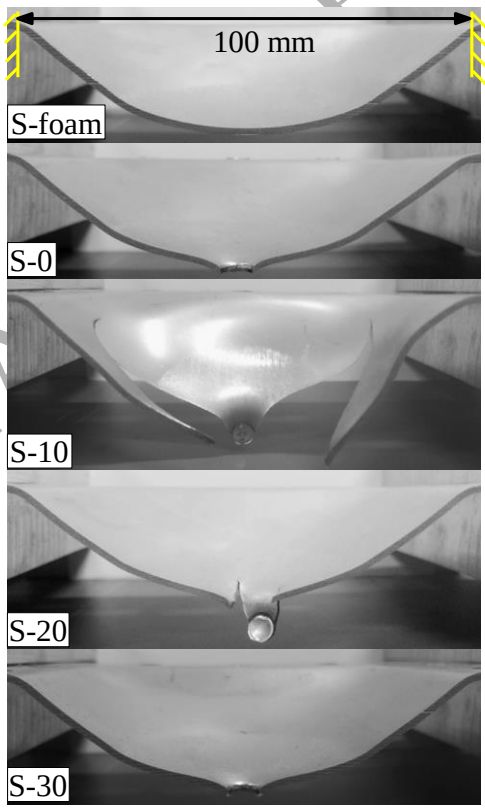

(a)

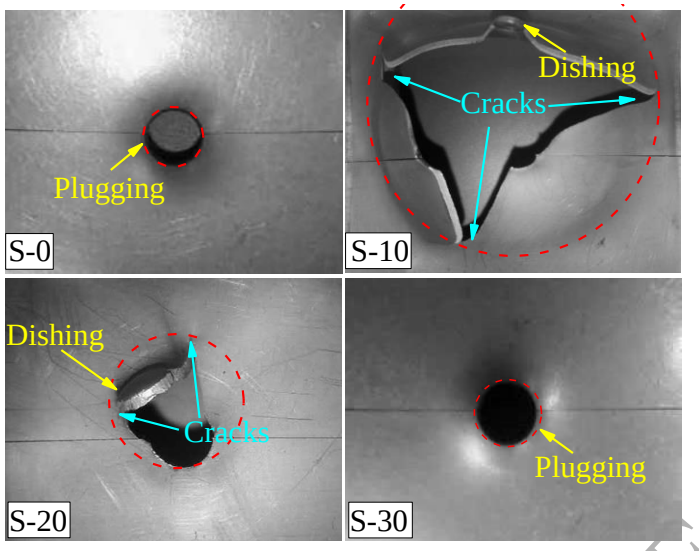

(b)

Fig. 9. Permanent deformation and failure of dynamically tested specimens: (a) cross-sectional view along diametrical plane and (b) plane view of local span.

Figure 9 presents the permanent deformation profiles and perforation modes of fully clamped monolithic plates subjected to foam projectile (S-foam, without FSP) and composite projectiles having identical initial impact velocity. The target plates are tested in order of increasing inner hole depth of the composite projectiles. All the plates exhibit similar blast-induced damage: bending and stretching with stationary plastic hinges at the radial position of $R = 28.5\,\text{mm}$ (centered at the impact site) and clamp supports, as shown in Fig. 9a. A comparison between the S-foam and other specimens indicates that the composite projectiles not only generate blast-induced damage, but also induce perforation on each plate. This demonstrates that the proposed composite projectile is capable of simulating combined blast and single fragment impact loading. Detailed perforation modes are presented in Fig. 9b. The perforation of S-0 and S-30 by FSP are dominated by plugging due to adiabatic shear failure of the target plates, while S-10 and S-20 are dominated by dishing and

cracking. Dishing and cracking happens in the following manner: the FSP induces the first crack of the target plate, then a strip of the plate is pushed to tear the plate in the extrusion direction from the first crack, during which new cracks form and propagate to the clamped edges. Further insight into S-10 and S-20 shows that the cracks in S-10 propagate much farther than those in S-20. The more significant cracks are caused by the enlarging of perforation hole by the foam projectile. This phenomenon is similar to the synergetic effect that has been reported: perforation caused by fragment will be aggravated by blast wave that follows [6]. Therefore, the present composite projectile is able to reveal the synergetic effect of blast and single fragment.

Figure 10 plots the central deflection and perforation diameter of the target plates as functions of arrival time interval between the foam projectile and the FSP. The errors are less than ± 1.78 mm. The perforation diameter is referred to the diameter of the external tangential circle that envelopes the whole region of the cracks, highlighted using red dashed lines in Fig. 9b. The most severe damage (*i.e.*, largest perforation diameter and central deflection) occurs in S-10, owing to further enlargement of the penetration hole by the foam projectile. On the contrary, specimens S-0 and S-30 are plugging-dominated and have the smallest penetration holes and deflections. Therefore, there exists a specific arrival time that results in the most severe damage, as shown in Fig. 10. A comparison between Fig. 9 and Fig. 10 shows that the most severe damage occurs when the perforation is dishing-dominated and the followed blast wave has enough momentum to aggravate the perforation.

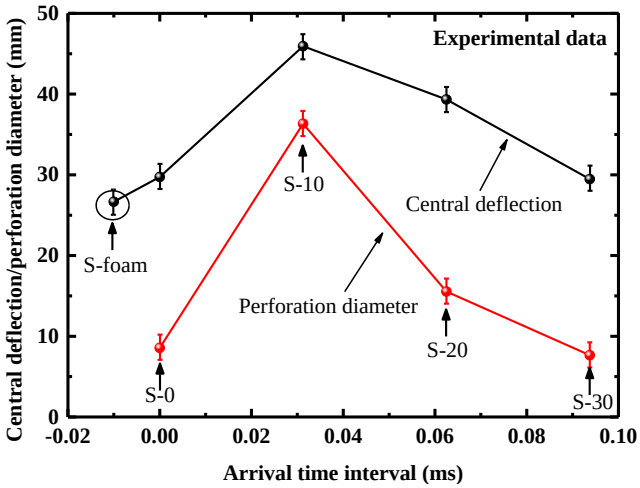

Fig. 10. Central deflection and perforation diameter of monolithic plates plotted as functions of arrival time interval. The errors are less than ± 1.78 mm.

Figure 11 plots the residual velocity of FSP as a function of arrival time interval between the foam projectile and the FSP. As the arrival time interval increases, the errors of the experimental measured residual velocities are $\pm 2.1\%, \pm 1.6\%, \pm 1.9\%$ and $\pm 3.2\%$, respectively, due to oblique shooting by high speed camera. It is interesting to find that the arrival time interval has significant effect on the residual velocity of FSP: as the arrival time interval is increased, the residual velocity first decreases, reaches a minimum, and then increases. Besides, comparison between Fig. 9 and Fig. 11 indicates that plugging-dominated perforations correspond to higher residual velocity while dishing-dominated perforations result in lower residual velocity. This finding actually reveals a new synergetic effect of combined blast and single fragment impact loading. Unlike the aforementioned synergetic effect which focuses on the damage of the target plate, the new synergetic effect focuses on the residual velocity of FSP. The arrival time interval affects significantly the residual velocity of FSP, and there exists a specific arrival time that results in the minimal residual velocity.

Physical mechanisms underlying such synergetic effect are explored in the section to follow.

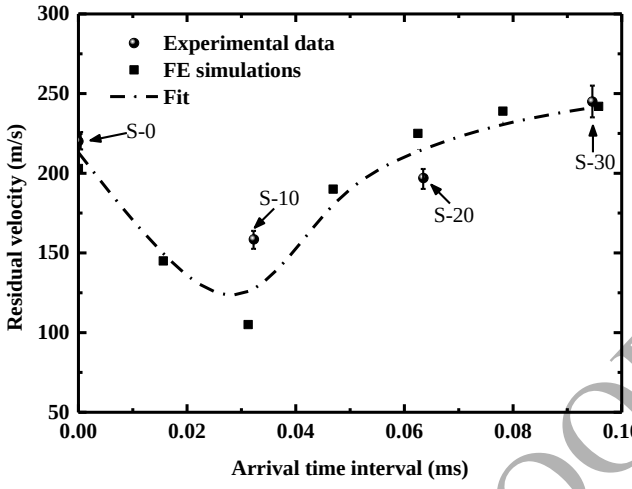

Fig. 11. Residual velocity of FSP versus arrival time interval: experimental measurements and FE simulations. As the arrival time interval increases, the errors of the measured residual velocities are ±2.1%,±1.6%,±1.9%and±3.2%, respectively.

5 Numerical modeling

Following the experimental investigation detailed above, numerical simulations with the method of finite elements are carried out to explore how the FSP is 'ejected' out of the inner hole of the metal foam projectile, and how the arrival time interval between the foam projectile and the FSP affects the residual velocity of the latter.

5.1 Finite element model

Full 3D (three-dimensional) FE simulations with LS-DYNA are performed to simulate the impact tests. Since both the composite projectile and target plate are axisymmetric about the longitudinal axis of the projectile, only a quarter of the

composite projectile and target plate is constructed, as shown in Fig. 12. Both are modeled using eight-node brick elements with reduced integration. The mesh size of the target plate is 0.5 mm in plane and 0.356 mm in thickness. As for the foam projectile, there are fifteen elements along the longitudinal axis and 12 elements around the quarter of the cylindrical circle. Along the radial direction, two mesh sizes are employed: from 0 to 4 mm the mesh size is 0.5 mm while from 4 mm to 28.5 mm the mesh size is 3.0265 mm. A global mesh size of 0.5 mm is used for the FSP. Mesh sensitivity study is carried out, showing that the current mesh size is sufficient to ensure numerical convergence.

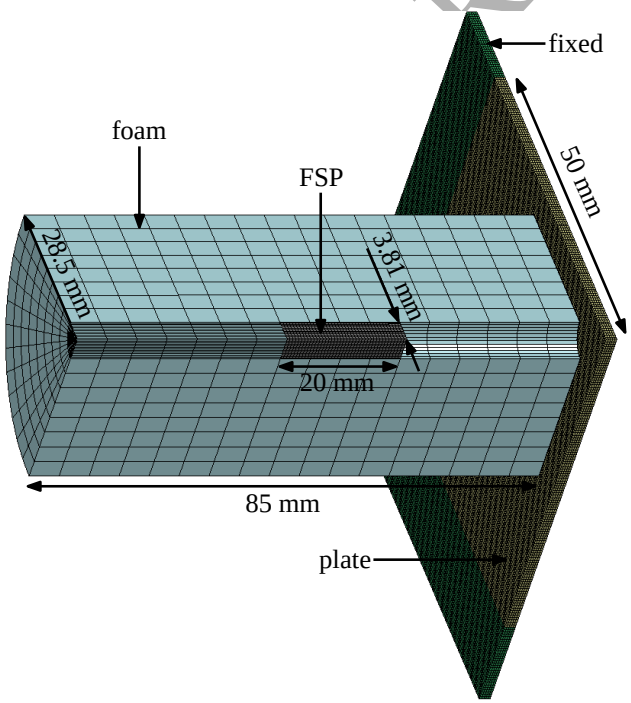

Fig. 12. A quarter of composite projectile and fully-clamped target plate: finite element model.

The materials involved in the simulation include hardened steel, closed-cell aluminum foam, and 304 stainless steel. Since little deformation of the FSP occurs during the impacting process, as shown in Fig. 5, a rigid material model MAT_RIGID

in LS-DYNA is adopted for the FSP. The metal foam projectile is modeled as an isotropic compressible continuum using the material model (MAT_CRUSHABLE_FOAM) with density of $\rho_f = 369$ kg/m^3. In the simulations, the foam is assumed to have a Young's modulus of 1.0 Gpa and a plastic Poisson's ratio of 0 [29]. The static yield stress versus volumetric strain is calibrated using the compressive stress versus strain curve shown in Fig. 6a. Since the dynamic compression strength of the foam projectile is mainly determined by inertial enhancement under impact velocity of approximately 320 m/s [30], the strain rate dependence of the foam material is not considered in the foam model. The material model for the target plate is MAT_MODIFIED_JOHNSON_COOK, expressed in a multiplicative form of strain, strain rate, and temperature, as given by:

$$\sigma_{eq} = \left(A + B\varepsilon_{eq}^{n}\right)\left(1 + \dot{\varepsilon}_{eq}^{*}\right)^{c}\left(1 - T^{*m}\right) \tag{15}$$

where σ_{eq} is the equivalent stress, ε_{eq} is the equivalent plastic strain, $\dot{\varepsilon}_{eq}^{*}$ is the normalized equivalent plastic strain rate defined as the ratio of equivalent strain rate ($\dot{\varepsilon}_{eq}$) to a user-defined strain rate value ($\dot{\varepsilon}_0$), n is the work hardening parameter, and A, B, c and m are material constants. In Eq. (15), $T^* = \left(T - T_r\right)/\left(T_m - T_r\right)$ where T is the absolute temperature, T_r is the room temperature, and T_m is the melting temperature typically set as the solidus temperature. The temperature increment due to adiabatic heating is calculated as:

$$\Delta T = \int_0^{\varepsilon_{eq}} \chi \frac{\sigma_{eq}}{\rho C_p} d\varepsilon_{eq} \tag{16}$$

where ρ is the material density, C_p is the specific heat, and χ is the Taylor-Quinney coefficient that gives the proportion of work converted into heat. The Cockcroft and Latham (CL) damage model is adopted as the fracture criterion in the modified Johnson-Cook (JC) model. The fracture criterion of the CL model is defined by the plastic work per unit volume, W, given by:

$$W = \int_0^{\varepsilon_{eq}} \sigma_1 d\varepsilon_{eq} \le W_{cr} \tag{17}$$

where σ_1 is the maximum principal stress. An element erode algorithm is implemented in the CL model, which erodes damaged elements whose W reaches its critical value, W_{cr}. The critical value can be determined according to Fig. 6b. In the present study, the material properties of 304 stainless steel used in [31] are adopted for the target plate, as listed in Table 2, while its fracture is determined by the measured stress versus strain curve (Fig. 6b).

Table 2

Material properties of 304 stainless steel [31].

Material property	Value
Density, ρ (kg/m^3)	7850
Young's modulus, E (GPa)	210
Poisson ratio, υ	0.33
A (MPa)	280
B (MPa)	805
c	0.27
m	1
n	0.622
χ	0.9
$\dot{\varepsilon}_0$ (s^{-1})	1×10^{-5}
C_p (J/kgK)	452
T_r (K)	293

T_m (K)	1763
The CL failure criterion, W_{cr} (MPa)	317

In the FE simulations, a segment based single surface contact algorithm is used between all the contacting surfaces. Since the effect of friction can be neglected for high velocity impact [32], friction between the FSP and the foam projectile is not defined in their contacts. Biaxial symmetric boundary conditions are applied. The target plate is fully clamped along the fixed region. A prescribed initial velocity V_0 is applied to the composite projectile.

5.2 Comparison of numerical results and experimental results

The simulated process of the FSP ejecting from the inner-hole of the foam projectile is displayed in Fig. 13. The ejection occurs at about 0.1 ms. Before 0.1 ms, the impact end of the foam projectile impinging on the target plate is crushed while the distal end of the foam projectile moves together with the FSP. After 0.1 ms, the FSP is 'ejected' from the inner hole and the plate is loaded simultaneously by both the foam projectile and the FSP. The simulated ejection process of the FSP and the deformation process of the target plate are consistent with the experimental observations discussed in the previous sections.

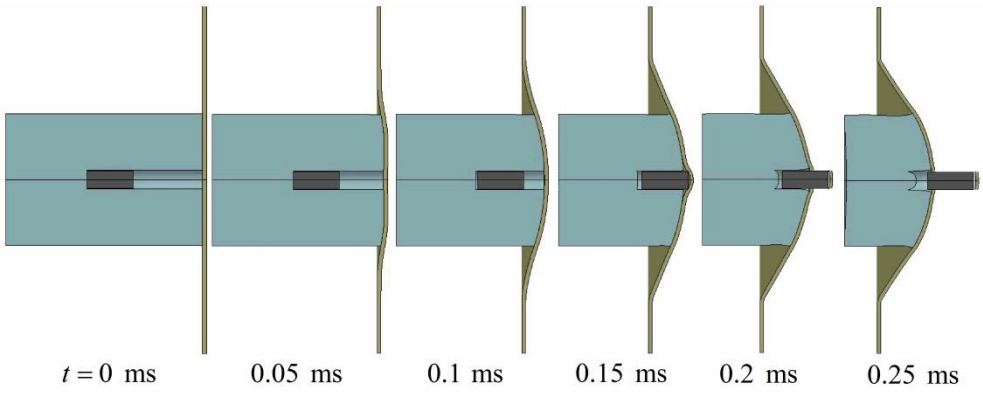

Fig. 13 Cross-sectional view of numerically simulated ejection process of the FSP and subsequent deformation and perforation process of fully-clamped target plate.

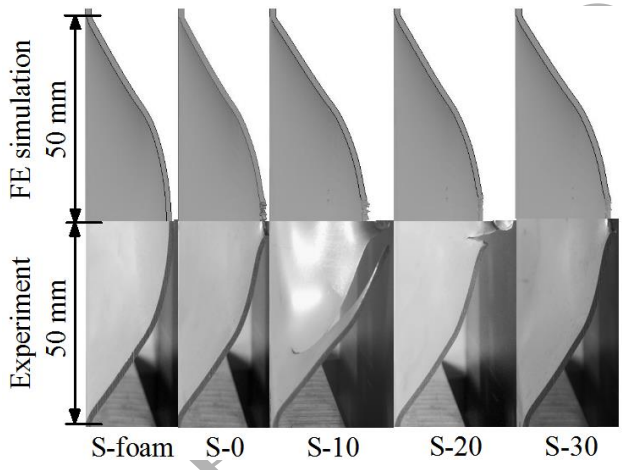

Fig. 14 Comparison between experimental and numerical permanent defection/failure modes of targets.

The residual velocity of FSP obtained from FE simulations is compared with that measured experimentally in Fig. 11. While the agreement in tendency is in general very good, there is difference between experiment and FE simulation at each depth of the inner hole (arrival time interval), especially for S-10 and S-20. To explore the reason of the difference, comparison of the permanent deflection/failure modes of the targets obtained experimentally and numerically is presented in Fig. 14. It is found that the FE simulations can well capture the permanent global deflection profiles of the targets but fail to capture all of the penetration modes. In the experiment,

asymmetric dishing modes exist for specimens S-10 and S-20, while in FE simulation, all of the perforation modes are shear plugging. The asymmetric dishing occurred in the tested 304 stainless steel plates may be caused by defects of the target's material and unevenness of the target, as analyzed in [31, 33]. Specifically, when the blunt-nosed projectile (used as FSP in the present test) impacts on the target, crack is initiated at one point on the target (this can be achieved by two ways, i.e. one is that defects exist in the target and the initial crack is initiated at the defected region; another is that the target is unevenness and the initial crack is initiated at the point of maximum stress). If the impact velocity is large enough to complete the circumferential crack within a short time, the penetration mode is shear plugging. Otherwise, the initiated crack will advance along the periphery of the contact area between blunt-nosed projectile and target until the ends of the crack are diametrically opposite, so the penetration mode is asymmetric dishing. In the present test, the difference between experiment and FE simulation for the residual velocity of the FSP at each inner hole depth can be attributed to the different penetration modes between experiment and FE simulation. Though all of the penetration modes are not captured, the variation trend of the numerically calculated residual velocity is in accordance with that measured in experiments, which is the primary focus of the present study. A fit of the data shown in Fig. 11 reveals that the variation trend of the residual velocity of the FSP is convex.

5.3 Physical mechanisms underlying the new synergetic effect

To explain the tendency of the residual velocity of the FSP (or the new synergetic effect) shown in Fig. 11, the prototypical problem underlies the observed new synergetic effect is put forward and analyzed, namely, ballistic penetration of a deforming plate wherein the deforming is caused by an impinging planar air blast $p_i(t)$, as sketched in Fig. 15. Unlike ballistic penetration of an un-deformed plate where the residual velocity depends on the material properties of both the projectile and target, the initial velocity V_0 and the configuration of target plate [34], ballistic penetration of a deforming plate depends on additional influencing factors: as the inner hole depth Δd varies, the relative velocities $V_0 - u(t)$ between the FSP and target plate are also different; as the target plate is pre-deformed by the foam projectile, the strain state and thickness of the central target plate is also different for different Δd due to bending and stretching, as shown in Fig. 15.

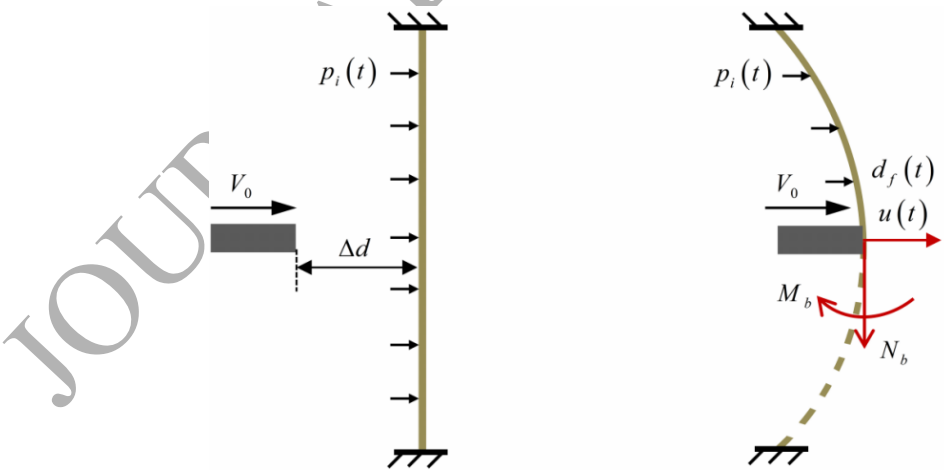

(a) (b)

Fig. 15. Ballistic penetration of a deforming plate: (a) at $t = 0$ and (b) at $t = t^{'}$ when FSP

makes contacts with the plate. With deformation assumed to exceed the yield strength of the plate material, M_b and N_b are the plastic bending moment and plastic stretching strength.

Following the above analysis, the mechanisms that how the influencing factors work are explored through detailed results of the numerical calculations. The velocity-time histories of the FSP and plug (target centre which is in contact with the front face of the FSP before plugging happens) for different inner hole depths are plotted in Fig. 16. As the inner hole depth (or arrival time interval) is increased, the variation trend of the effective penetration velocity (relative velocity between the FSP and plug) initially decreases then increases: 320 m/s, 214 m/s, 176 m/s and 224 m/s. Besides, the moving state of the targets is also different (for $\Delta d = 0,10$ mm, the velocity of the target centre is on its rising stage when the FSP impacts on the target, but for $\Delta d = 20,30$ mm, the velocity of the target centre is on its descending stage). As a result of which, the interaction time between the FSP and the target centre (or the plug after penetration) initially increases then decreases: 0.055 ms, 0.135 ms, 0.053 ms, 0.043 ms. For a blunt projectile (used as FSP in the paper for simplicity) impacts on the target, the penetration mode of the target is shear plugging and associated global bending and stretching. As the interaction time between the FSP and the target centre increases, the shear plugging is delayed while the global bending and stretching of the target goes on. During the delayed interaction time, more kinetic energy of the FSP is consumed by the resistance provided to the FSP, as shown in Fig. 17, in which contact pressure-time histories between the FSP and the target centre for different inner hole depths are provided. As the inner hole depth is increased, the consumed

kinetic energy of the FSP is initially increasing then decreasing, thus the residual velocity of the FSP should be initially decreasing then increasing, which is in accordance with the results shown in Fig. 11. Since the underlying mechanism analyzed here is associated with the relative motion between the FSP and the target, this influencing factor (or explanation) is named as 'motion-factor'.

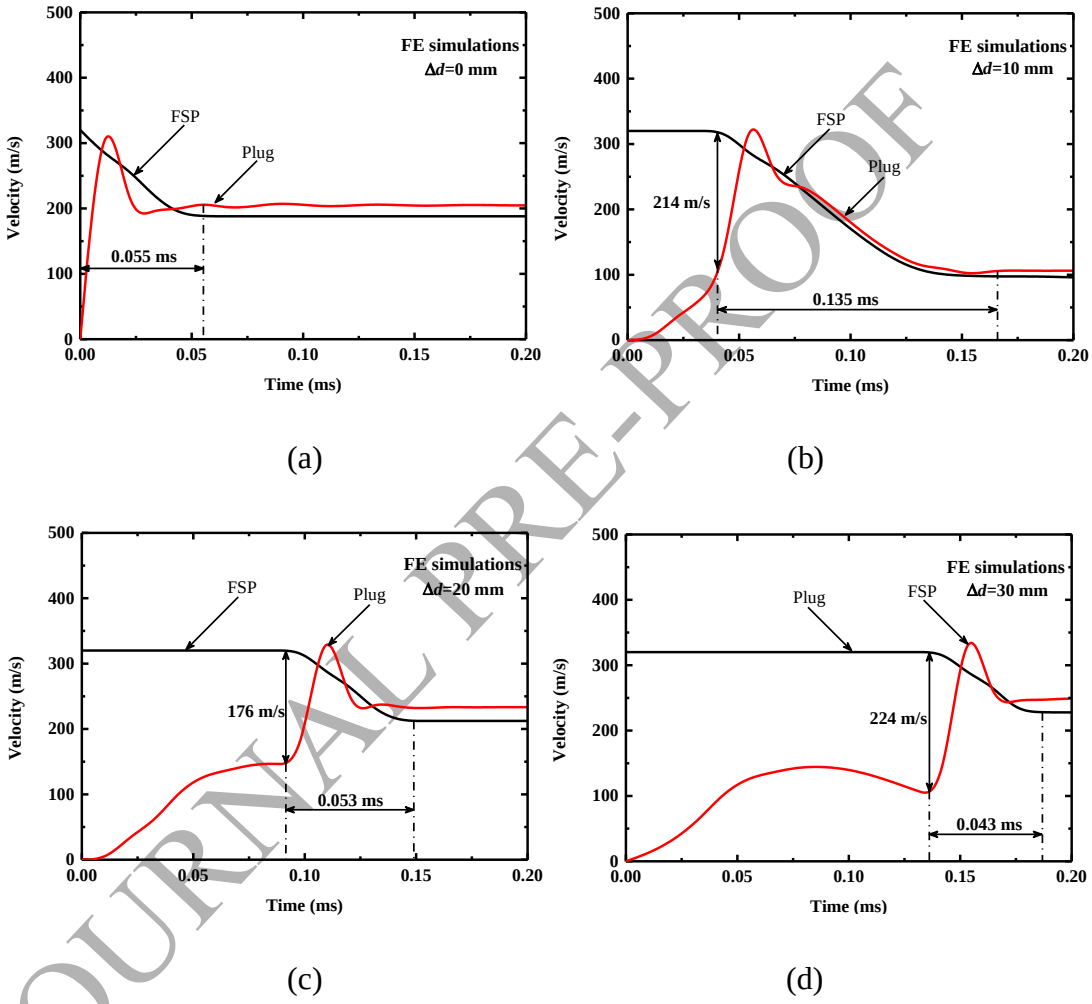

Fig. 16. Velocity-time histories of FSP and plug obtained from FE simulations for selected values of inner hole depth: $\Delta d = 0$, 10, 20 and 30 mm.

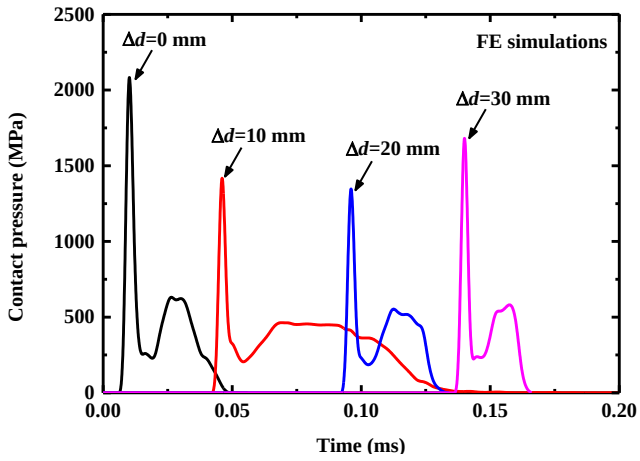

Fig. 17. Contact pressure-time histories between the FSP and the target for different inner hole depths.

From Figs. 8 and 13, it is seen that the FSP actually impacts on a deformed target. A deformed target differs from an un-deformed one in two ways: one is that a deformed target is thinned due to stretching; another is that a deformed target has a different strain state (or stress state). Fig. 18 presents the strain state of the deformed plate at the instant when the FSP contacts the plate for different inner hole depths. As the inner hole depth is increased, the effective strain at the plate center is also increased. According to the CL model, material failure occurs when the plastic work per unit volume exceeds a critical value, W_{cr}. For a deformed plate, a portion of the plastic work (W_{foam}) is consumed by stretching of the plate which is induced by impact of foam projectile. The rest of the plastic work ($W_{cr} - W_{foam}$) is then used to resist the plugging. As a result, the larger the deflection the smaller the rest of the plastic work, thus less resistance is provided to the FSP in the plugging process. Besides, as the inner hole depth is increased, more impulse is transmitted to the plate prior to the FSP's arrival, which leads to larger overall deflection of the target plate and thinner

thickness of the target plate. When the FSP impacts on a thinner target plate, a thinner plug is 'ejected' form the target centre, thus smaller inertia resistance is provided to the FSP by the target centre (plug). Therefore, as the inner hole depth is increased, the resistance provided to the FSP from both inertia resistance and plugging resistance will decrease, which leads to increase in residual velocity. Since the underlying mechanism analyzed here is associated with material and thickness of the target plate, this explanation (or influencing factor) is named as 'target-factor'.

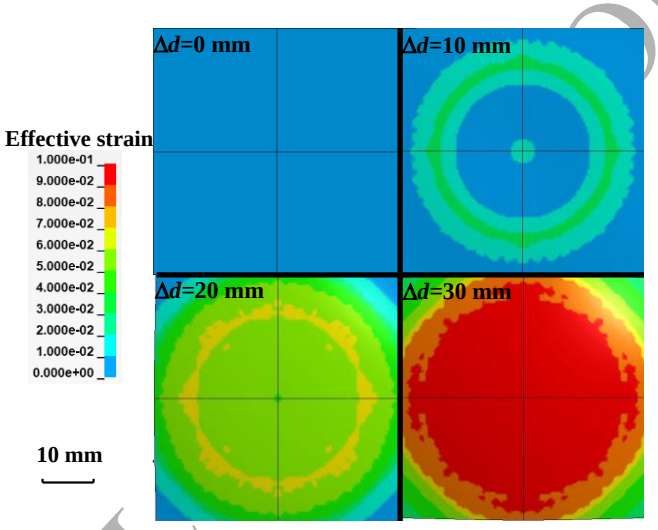

Fig. 18. Simulated stress state in central portion of target plate subjected to composite projectile of different inner hole depths at the instant just before the FSP impacts on the plate.

From the above mechanical analysis, the tendency of residual velocity shown in Fig. 11 may have been associated with two influencing factors: motion-factor and target-factor. Since the tendency of residual velocity of the FSP is in accordance with the motion-factor while contradictory to the target-factor, we can infer that the motion-factor is dominant in determining the tendency of the residual velocity while the target-factor has less influence. It should be noted that this inference depends upon that motion-factor and target-factor are the only influencing factors. Actually, Strain

hardening and strain rate sensitivity may also have influence on the residual velocity of the FSP. Since the aim of the present study is to propose a new experimental tool, further investigation of the prototypical problem associated with the experiments will be undertaken in a following study.

6 Concluding remarks

A novel composite projectile for simulating combined blast and single fragment impact loading has been proposed. The technique is laboratory and convenient for exploring the protective properties of structures subjected to combined blast and single fragment impact loading. Validation of the technique is demonstrated by theoretical modeling and numerical simulation, and its feasibility is verified experimentally with normal impact tests of clamped plates by composite projectiles. Main conclusions drawn from the study are:

- Comparison of the predicted combined loadings from cased explosives and composite projectiles shows that under certain conditions the composite-projectile-based approach can be used to simulate combined loadings from cased explosives.
- Experimental results show that the composite projectile is able to generate both blast-induced deflection and fragment-induced perforation on fully clamped plate.
- The arrival time interval of blast and fragment loading has significant effect on the deformation and perforation of the plate as well as the new synergetic effect

of blast and fragment loading on the residual velocity of the FSP.

- The prototypical problem underlying the new synergetic effect is the ballistic penetration of a deforming plate wherein the deforming is caused by an impinging planar air blast.

- The proposed experimental technique only considers one fragment, thus the group thrust by fragments cluster that occurs in real explosion circumstances is yet simulated. Still, the technique provides a useful approach to value the resistance of structures subjected to combined blast and single fragment impact loading, especially to explore the physical mechanisms underlying such combined loadings.

Acknowledgments

This work was supported by the National Key Research and Development Program of China (2017YFB1102801), the Open Project for Key Laboratory of Intense Dynamic Loading and Effect (KLIDLE1801), the National Natural Science Foundation of Chin a (11472209, 11472208 and 11572087), the Aviation Science Foundation Project(201 70970002), China Postdoctoral Science Foundation (2016M600782), and the Open Fu nd of the State Key Laboratory of Mechanics and Control of Mechanical Structures （Nanjing University of Aeronautics and astronautics）(MCMS-E0219K02).

References

[1] Arnold J L, Halpern P, Tsai M C, *et al.* Mass casualty terrorist bombings: a comparison of outcomes by bombing type. Ann. Emerg. Med., 2004, 43: 263-73.

[2] Elsayed N M, Gorbunov N V, Elsayed, *et al.* Explosion and blast-related injuries:effects of explosion and blast from military operations and acts of terrorism. Elsevier/Academic Press.

[3] Wallace D. Improvised explosive devices and traumatic brain injury: the military experience in iraq and afghanistan. Australasian Psychiatry Bulletin of Royal Australian & New Zealand College of Psychiatrists, 2009, 17, 218.

[4] Kong X S, Wu W G, Li J, *et al*. Experimental and numerical investigation on a multi-layer protective structure under the synergistic effect of blast and fragment loadings. Int. J. Impact Eng., 2009, 65: 146-162.

[5] Grisaro H Y, Dancygier A N. Characteristics of combined blast and fragment loading. Int. J. Impact Eng., 2018, 116: 51-64.

[6] Nyström U, Gylltoft K. Numerical studies of the combined effects of blast and fragment loading. Int. J. Impact Eng., 2009, 36: 995-1005.

[7] Ranwaha N, Yuen S C K. The effects of blast-induced fragments on cellular materials. Int. J. Impact Eng., 2016, 92: 50-65.

[8] Ebrahimi H, Ghosh R, Mahdi E, *et al.* Honeycomb sandwich plates subjected to combined shock and projectile impact. Int. J. Impact Eng., 2016, 95: 1-11.

[9] Zhang C, Cheng Y, Zhang P, *et al*. Numerical investigation of the response of I-core sandwich plates subjected to combined blast and fragment loading. Eng. Struct., 2017, 115: 459-471.

[10] Li M, Zhu X, Hou H L, *et al*. Numerical simulation of steel plates subjected to the impact of both impact waves and fragments. Chinese Journal of Ship Research, 2015, 10: 60-67.

[11] Rakvg K G, Underwood N J, Schleyer G K, *et al*. Transient pressure loading of clamped metallic plates with pre-formed holes. Int. J. Impact Eng., 2013, 53: 44-55.

[12] Radford D D, Deshpande V S, Fleck N A. The use of metal foam projectiles to simulate shock loading on a structure. Int. J. Impact Eng., 2005, 31: 1152-1171.

[13] Rathbun H J, Radford D D, Xue Z, *et al*. Performance of metallic honeycomb-core sandwich

beams under shock loading. Int. J. Solids Struct., 2006, 43: 1746-1763.

[14] McShane G J, Radford D D, Deshpande V S, *et al*. The response of clamped sandwich plates with lattice cores subjected to shock loading. Eur. J. Mech. A/Solids, 2006, 25: 215-229.

[15] Radford D D, Fleck N A, Deshpande V S. The response of clamped sandwich beams subjected to shock loading. Int. J. Impact Eng., 2006, 32: 968-987.

[16] Yahaya M A, Ruan D, Lu G, *et al*. Response of aluminium honeycomb sandwich plates subjected to foam projectile impact-An experimental study. Int. J. Impact Eng., 2015, 75: 100-109.

[17] Park S, Uth T, Fleck N A, *et al*. Sand column impact onto a kolsky pressure bar. Int. J. Impact Eng., 2013, 62: 229-242.

[18] Russell B P, Liu T, Fleck N A, *et al*. The soft impact of composite sandwich beams with a square-honeycomb core. Int. J. Impact Eng., 2012, 48: 65-81.

[19] Uth T, Deshpande V S. Response of clamped sandwich beams subjected to high-velocity impact by sand slugs. Int. J. Impact Eng., 2014, 69: 165-181.

[20] Goel A, Uth T, Wadley H N G, *et al*. Effect of surface properties on momentum transfer to targets impacted by high-velocity sand slugs. Int. J. Impact Eng., 2017, 103: 90-106.

[21] Mays G C, Smith P D. Blast Effects on Buildings - (2nd Edition), Thomas Telford, London, England, 2009.

[22] Baker W E. Explosions in air. Austin (TX, US): University of Texas Press; 1973: 285.

[23] U.S. Army. Fundamentals of protective design for conventional weapons. Technical Manual TM 5-855-1; 1992: 271.

[24] Henrych J, Abrahamson G R. The Dynamics of Explosion and Its Use. Elsevier Scientific Pub. Co. ; 1979: 218.

[25] Hutchinson M D.The escape of blast from fragmenting munitions casings. Int. J. Impact Eng., 2009, 36: 185-192.

[26] Curran D R. Simple fragment size and shape distribution formulae for explosively fragmenting munitions. Int. J. Impact Eng., 1997, 20: 197-208.

[27] Gurney R W. The Initial Velocities of Fragments from Bombs, Shell and Grenades, 1943.

[28] He S Y, Zhang Y, Dai G, *et al*. Preparation of density-graded aluminum foam. Mat. Sci. Eng. A-Struct., 2014, 618: 496-499.

[29] Ashby M F, Evans A G, Fleck N A, *et al*. Metal Foams: A Design Guide. Butterworth-Heinemann, Oxford, 2002.

[30] Li L, Xue P, Luo G. A numerical study on deformation mode and strength enhancement of metal foam under dynamic loading. Mater. Design, 2016, 110: 72-79.

[31] Frontán J, Zhang Y, Ming D. Ballistic performance of nanocrystalline and nanotwinned ultrafine crystal steel. Acta Mater., 2012, 60: 1353-1367.

[32] Børvik T, Hopperstad O S, Berstad T. Numerical simulation of plugging failure in ballistic penetration. Int. J. Solids Struct., 2001, 38: 6241-6264.

[33] Russell, B P. Multi-hit ballistic damage characterisation of 304 stainless steel plates with finite elements. Mater. Design, 2014, 58: 252-264.

[34] Børvik T, Langseth M, Hopperstad O S. Ballistic penetration of steel plates. Int. J. Impact Eng.,1999, 22: 855-886.